Search for dark photons from Higgs boson decays via *ZH* production with a photon plus missing transverse momentum signature from *p p* collisions at √*s* = 13 TeV with the ATLAS detector

The ATLAS Collaboration

This paper describes a search for dark photons (γ_d) in proton-proton collisions at $\sqrt{s}$ = 13 TeV at the Large Hadron Collider (LHC). The dark photons are searched for in the decay of Higgs bosons ($H \rightarrow \gamma\gamma_d$) produced through the ZH production mode. The transverse mass of the system, made of the photon and the missing transverse momentum from the non-interacting γ_d, presents a distinctive signature as it peaks near the Higgs boson mass. The results presented use the total Run-2 integrated luminosity of 139 fb^{-1} recorded by the ATLAS detector at the LHC. The dominant reducible background processes are estimated using data-driven techniques. A Boosted Decision Tree technique is adopted to enhance the sensitivity of the search. As no excess is observed with respect to the Standard Model prediction, an observed (expected) upper limit on the branching ratio BR($H \rightarrow \gamma\gamma_d$) of 2.28% (2.82$^{+1.33}_{-0.84}$%) is set at 95% CL for massless γ_d. For massive dark photons up to 40 GeV, the observed (expected) upper limits on BR($H \rightarrow \gamma\gamma_d$) at 95% confidence level is found within the [2.19,2.52]% ([2.71,3.11]%) range.

Contents

1 Introduction

There is strong astrophysical evidence suggesting the existence of dark matter (DM) with a density about five times higher than ordinary baryonic matter [1]. However, its fundamental nature is unknown and it is plausible that it is a component of a larger "dark sector", which couples weakly to the Standard Model (SM) and possesses a rich internal structure and interactions. Existing models propose dark sectors that contain few or many particles, some providing ideal candidates for DM. The interaction of these dark states can be Yukawa-like or mediated by dark gauge bosons or both.

The dark and visible sectors may interact through a portal offering a potential experimental signature. The form of this portal can be classified according to the type and dimension of its operators. The best motivated and most studied cases contain relevant operators taking different forms, depending on the spin of the mediator: vector (spin 1), neutrino (spin 1/2), Higgs boson (scalar) and axion (pseudo-scalar) [2].

The vector portal considered in this paper is the one where the interaction results from the kinetic mixing between one dark and one visible Abelian gauge boson. The visible photon is taken to be the boson of the $U(1)$ gauge group of electromagnetism—or the hyper-charge in the regime above the electroweak symmetry breaking scale—and the dark photon (γ_d) is identified as the boson of an extra $U(1)_D$ gauge group of the dark sector. This mixing is always possible because the field strengths of two Abelian gauge fields can be multiplied together to give a dimension four operator [3]. The existence of such an operator means that the two gauge bosons mix as they propagate [4]. This kinetic mixing provides the portal linking the dark and visible sectors and makes the experimental detection of the dark photon possible.

Massless and massive dark photons, whose theoretical frameworks as well as experimental signatures are quite distinct, give rise to dark sectors with different phenomenological and experimental features. The massive dark photon has received so far most of the attention because it couples directly to the SM currents and is more readily accessible in the experimental searches [5–9]. The massless dark photon arises from a sound theoretical framework [2]. It does not couple directly to any of the SM currents and interacts instead with ordinary matter only through operators of dimension higher than four. It provides, with respect to the massive case, a comparably rich, if perhaps more challenging, experimental target.

Looking beyond particle physics and towards cosmology, dark photons may solve the small-scale structure formation problems [10]. In astroparticle physics, dark photons may induce the Sommerfeld enhancement of the DM annihilation cross-section needed to explain the PAMELA-Fermi-AMS2 positron anomaly [11]. They may also assist light DM annihilation to reach the phenomenologically required magnitude, and make asymmetric DM scenarios phenomenologically viable [12, 13].

This analysis searches for dark photons predicted by a new model generating exponentially spread SM Yukawa couplings from unbroken $U(1)_D$ quantum numbers in the dark sector [14]. In this approach, non-perturbative flavour- and chiral-symmetry breaking is transferred from the dark to the visible sector via heavy scalar messenger fields that might produce new physics signals at the Large Hadron Collider (LHC). For massless dark photons, the $U(1)_D$ kinetic mixing with $U(1)$ can be tuned away on shell, in agreement with all existing constraints [15, 16], while off-shell contributions give rise to higher-dimensional contact operators strongly suppressed by the scale of the heavy messenger mass.

A potential discovery process for dark photons proceeding via Higgs-boson production at the LHC is presented in this paper. Thanks to the non-decoupling properties of the Higgs boson, a branching ratio of $H \rightarrow \gamma\gamma_d$ with values up to a few percent are possible for a massless dark photon as well as for heavy dark-sector scenarios [12–14]. The corresponding signature consists, for a Higgs boson with a mass

$m_H = 125$ GeV, of a photon with an energy $E_\gamma = m_H/2$ in the Higgs centre-of-mass frame and a similar amount of missing transverse momentum (E_T^{miss}) which originates from the escaping γ_d [13].

Moreover, in the unbroken $U(1)_D$ scenarios, the two-body decay $H \to \gamma\gamma_d$ can be enhanced despite existing theoretical constraints [12], providing a very distinctive signature of a single photon plus missing transverse momentum at the Higgs boson mass resonance. If such a signature is discovered at the LHC, CP invariance will imply the spin-1 nature of the missing particle, excluding axions or other ultra light scalar particles.

The photon plus E_T^{miss} signature has been extensively studied by the LHC experiments [17–19]. In the particular case of massless γ_d, searches in Higgs boson decays were performed at the LHC in pp collisions at a centre-of-mass energy of 13 TeV. The CMS experiment has probed this decay channel using Higgs boson events produced in association with a Z boson $ZH(Z \to \ell^+\ell^-)$ with an integrated luminosity of 137 fb^{-1} [20], or via vector-boson fusion (VBF) production [21] (with 130 fb^{-1}) setting an observed (expected) upper limit on the BR($H \to \gamma\gamma_d$) at the 95% confidence level (CL) of 4.6% (3.6%) and 3.5% (2.8%) respectively. ATLAS has set an observed (expected) limit on the $H \to \gamma\gamma_d$ branching ratio, using the VBF production mode with an integrated luminosity of 139 fb^{-1}, to 1.8% (1.7%) at the 95% CL [22].

This analysis is based on the ZH production mode where $Z \to \ell^+\ell^-$ ($\ell = e, \mu$) and $H \to \gamma\gamma_d$, which proceeds at leading order through the Feynman diagrams shown in Figure 1. The study is performed using a final state consisting of two same-flavour, opposite-charge electrons or muons, an isolated photon and missing transverse momentum. The requirements applied to the photon and the E_T^{miss}, originating from a potential SM Higgs boson decay, are optimised to maximise the signal acceptance. The leptons, on the other hand, are used for triggering on the event and provide a Z boson mass constraint. The transverse mass m_T of the $\gamma - E_T^{\text{miss}}$ system presents a kinematic edge at the Higgs boson mass and is included as a variable of interest in the boosted decision tree (BDT) score that is exploited to search for a dark photon signal. The kinematics of these events allow the search for low-mass ($\neq 0$) γ_d. Hence, the analysis is optimized for dark photon searches in the [0-40] GeV mass range.
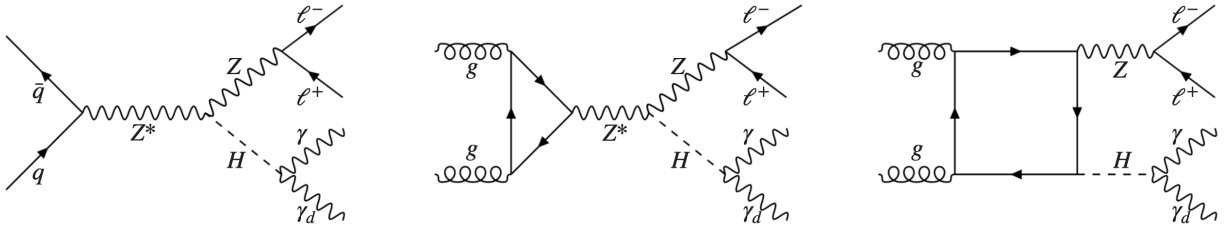

Figure 1: Feynman diagrams for H$\to \gamma\gamma_d$ in $q\bar{q} \to ZH$ and $gg \to ZH$ production modes.

2 The ATLAS detector

The ATLAS detector [23] at the LHC covers nearly the entire solid angle around the collision point[1]. It consists of an inner tracking detector surrounded by a thin superconducting solenoid, electromagnetic and

---

[1] ATLAS uses a right-handed coordinate system with its origin at the nominal interaction point (IP) in the centre of the detector and the z-axis along the beam pipe. The x-axis points from the IP to the centre of the LHC ring, and the y-axis points upwards. Cylindrical coordinates (r, ϕ) are used in the transverse plane, ϕ being the azimuthal angle around the z-axis. The pseudorapidity is defined in terms of the polar angle θ as $\eta = -\ln\tan(\theta/2)$. Angular distance is measured in units of $\Delta R \equiv \sqrt{(\Delta\eta)^2 + (\Delta\phi)^2}$.

hadron calorimeters as well as a muon spectrometer incorporating three large superconducting air-core toroidal magnets.

The inner-detector system (ID) is immersed in a 2 T axial magnetic field and provides charged-particle tracking in the range of pseudorapidity $|\eta| < 2.5$. The high-granularity silicon pixel detector covers the vertex region and typically provides four measurements per track, the first hit normally being in the insertable B-layer (IBL) installed before Run 2 [24, 25]. It is followed by the silicon microstrip tracker (SCT), which usually provides eight measurements per track. These silicon detectors are complemented by the transition radiation tracker (TRT), which enables radially extended track reconstruction up to $|\eta| = 2.0$. The TRT also provides electron identification information based on the fraction of hits (typically 30 in total) above a higher energy-deposit threshold corresponding to transition radiation.

The calorimeter system covers the pseudorapidity range $|\eta| < 4.9$. Within the region $|\eta| < 3.2$, electromagnetic (EM) calorimetry is provided by barrel and endcap high-granularity lead/liquid-argon (LAr) calorimeters, with an additional thin LAr presampler covering $|\eta| < 1.8$ to correct for energy loss in material upstream of the calorimeters. Hadron calorimetry is provided by the steel/scintillator-tile calorimeter, segmented into three barrel structures within $|\eta| < 1.7$, and two copper/LAr hadron endcap calorimeters. The solid angle coverage is completed with forward copper/LAr and tungsten/LAr calorimeter modules optimised for electromagnetic and hadronic energy measurements respectively.

The muon spectrometer (MS) comprises separate trigger and high-precision tracking chambers measuring the deflection of muons in a magnetic field generated by the superconducting air-core toroidal magnets. The field integral of the toroids ranges between 2.0 and 6.0 T m across most of the detector. Three layers of precision chambers, each consisting of layers of monitored drift tubes, covers the region $|\eta| < 2.7$, complemented by cathode-strip chambers in the forward region, where the background is highest. The muon trigger system covers the range $|\eta| < 2.4$ with resistive-plate chambers in the barrel, and thin-gap chambers in the endcap regions.

Interesting events are selected by the first-level trigger system implemented in custom hardware, followed by selections made by algorithms implemented in software in the high-level trigger [26]. The first-level trigger selects events from the 40 MHz bunch crossings at a rate below 100 kHz, which the high-level trigger further reduces in order to record events to disk at about 1 kHz. An extensive software suite [27] is used in the reconstruction and analysis of real and simulated data, in detector operations and in the trigger and data acquisition systems of the experiment.

3 Data samples

The data used in this paper were collected by the ATLAS experiment from the LHC pp collisions at $\sqrt{s} = 13$ TeV during stable beam conditions, with all subdetectors operational [28]. The corresponding total integrated luminosity is 139 fb^{-1}. The data were recorded with high efficiency using unprescaled trigger algorithms based on the presence of single leptons or di-leptons, where electrons and muons are considered as leptons [29, 30].

The trigger thresholds are based on the transverse momentum p_T of the leptons and are determined by the data-taking conditions during the different periods [31], particularly by the number of multiple pp interactions in the same or neighbouring bunch crossings, referred to as pile-up. The number of pile-up interactions ranges from about 8 to 70, with an average of 34. Single-lepton triggers with low p_T threshold and lepton isolation requirements are combined in a logical OR with higher-threshold triggers

without isolation requirements to give maximum efficiency. The di-lepton triggers require two leptons that satisfy loose identification criteria, with symmetric (symmetric or asymmetric) p_T thresholds for electrons (muons). The di-lepton trigger complements the single-lepton trigger to recover between 3% and 3.6% signal efficiency depending on the dark photon mass points for combined $Z \rightarrow ee$ and $Z \rightarrow \mu\mu$ final states.

4 Simulated event samples

Monte Carlo (MC) simulated samples are used to model both the signal and the different background processes using the configurations shown in Table 1. All the samples were generated at a centre-of-mass energy of 13 TeV. The generated events were processed through a simulation [32] of the ATLAS detector geometry and response using Geant4 [33], and through the same reconstruction software as the collected pp collision data. Corrections were applied to the simulated events so that the particle candidates' selection efficiencies, energy scales and energy resolutions match those determined from data control samples. In addition, appropriate scale factors corresponding to the fired triggers are applied [29, 30]. The simulated samples are normalised to the total integrated luminosity, using the corresponding cross-sections computed to the highest order available in perturbation theory. The pile-up effects were modelled using events from minimum-bias interactions generated using Pythia8.186 [34] with the A3 set of tuned parameters [35]. They were overlaid onto the simulated hard-scatter events according to the luminosity profile of the recorded data (reweighting procedure). For massive γ_d signal samples and the $tW\gamma$ background process, the detector response was simulated using a fast parameterized simulation of the ATLAS calorimeters [36]. For the massless signal samples and all remaining background samples, the full Geant4 simulation was used. All simulated samples, except those produced with the Sherpa2.2.1 [37] event generator, used EvtGen 1.2.0 [38] to model the decays of heavy-flavour hadrons.

4.1 Signal samples

The signal process of a Higgs boson decaying to a photon and an invisible dark photon (γ_d) was generated in the ZH production mode as shown in Figure 1. Both $q\bar{q} \rightarrow ZH$ and $gg \rightarrow ZH$ production modes were considered in order to have the full ZH cross-section of 0.884 pb [39]. Matrix elements were estimatd using Powhegv2 [40, 41] with the NNPDF3.0 parton density libraries [42]. Events from the $q\bar{q} \rightarrow ZH$ process were generated at next-to-leading order (NLO) while the ones corresponding to $gg \rightarrow ZH$ were generated at leading order (LO). Pythia8.245 was used to perform the Higgs boson decay as well as the hadronisation and showering with the CTEQ6L1 PDF set and the AZNLO tune [43]. The samples were generated at a Higgs boson mass of 125 GeV, a width set to the SM value of 4 MeV [39] and the complex pole scheme [44] turned off. The Hidden Valley scenario [45] for BSM Higgs boson decay as implemented in Pythia8.150 was used to produce $H \rightarrow \gamma\gamma_d$ signal events. A total of six Monte Carlo samples were generated with dark photon masses equal to 0, 1, 10, 20, 30, 40 GeV. Finally, in order to increase the generation efficiency, a generator-level lepton filter was applied, requiring two electrons or muons with $p_T > 10$ GeV and $|\eta| < 2.7$.

Table 1: The configurations used for event generation of signal and background processes. *V* refers to an electroweak boson (*W* or Z/γ^*). The matrix element (ME) order refers to the order in the strong coupling constant of the perturbative calculation in the MC event generation. PDF refers to the parton density librairies used with the generator. The tune refers to the underlying-event tune of the parton shower model.

Process	Generator	ME Order	PDF	Parton Shower	Tune
		Signal samples			
$ZH, H \rightarrow \gamma\gamma_d$	Powheg Box v2	NLO	NNPDF3.0NLO	Pythia 8.245	AZNLO
		SM background samples			
$V\gamma^{QCD}$	Sherpa v2.2.8	NLO (up to 2 jets), LO (up to 3 jets)	NNPDF3.0NNLO	Sherpa MEPS@NLO	Sherpa
$V\gamma^{EWK}$	MadGraph5_aMC@NLO [v2.6.5]	LO	NNPDF2.3LO	Pythia 8.240	A14
Z^{QCD}	Sherpa v2.2.1	NLO (up to 2 jets), LO (up to 4 jets)	NNPDF3.0NNLO	Sherpa MEPS@NLO	Sherpa
Z^{EWK}	Sherpa v2.2.1	NLO (up to 2 jets), LO (up to 4 jets)	NNPDF3.0NNLO	Sherpa MEPS@NLO	Sherpa
Single t-quark/$t\bar{t}$	Powheg Box v2	NLO	NNPDF2.3LO	Pythia 8.230	A14
$t\bar{t}$ (V, VV), $Wt\gamma$	MadGraph5_aMC@NLO [v2.2.3]	NLO	NNPDF2.3LO	Pythia 8.210	A14
SM Higgs	Powheg Box v2	NNLO (ggF), NLO (VBF, $VH, t\bar{t}H$)	PDF4LHC15	Pythia 8.230	AZNLO
$VV\gamma$	Sherpa v2.2.11	NLO (0 jets), LO (up to 3 jets)	NNPDF3.0NNLO	Sherpa MEPS@NLO	Sherpa
VV/VVV	Sherpa v2.2.2	NLO (0 jets), LO (up to 3 jets)	NNPDF3.0NNLO	Sherpa MEPS@NLO	Sherpa
		Samples for evaluating systematic uncertainties			
$ZH, H \rightarrow \gamma\gamma_d$	Powheg Box v2	NLO	NNPDF3.0NLO	Herwig v7.1.3	H7-UE-MMHT
$Z\gamma^{QCD}$	MadGraph5_aMC@NLO [v2.3.3]	NLO	NNPDF2.3LO	Pythia 8.212	A14
$W\gamma^{QCD}$	MadGraph [v2.8.1]	NLO	NNPDF2.3LO	Pythia 8.244	A14
$W\gamma^{EWK}$	MadGraph [v2.8.1]	NLO	NNPDF3.0NLO	Herwig v7.1.3	H7-UE-MMHT
Z^{QCD}	MadGraph5_aMC@NLO [v2.2.3]	NLO	NNPDF2.3LO	Pythia 8.210	A14
Z^{EWK}	Herwig v7.1.3	NLO	NNPDF3.0NLO	Herwig v7.1.3	H7-UE-MMHT
$V\gamma\gamma$	MadGraph5_aMC@NLO [v2.7.3]	NLO	NNPDF2.3LO	Pythia 8.244	A14
$t\bar{t}$	Powheg Box v2	NLO	NNPDF3.0NLO	Herwig v7.0.4	H7-UE-MMHT
$t\bar{t}V$	MadGraph5_aMC@NLO [v2.3.3]	NLO	NNPDF3.0NLO	Herwig v7.2.1	H7-UE-MMHT

4.2 Background samples

The analysis is affected by a large variety of background processes. The irreducible background comes from $VV\gamma$ final states (V being any of W, Z) with both V bosons decaying leptonically. The reducible background, which is dominant, comes from biased E_T^miss measurement (fake E_T^miss) — typically due to undetected particles or hadronic jets not fully contained in the detector acceptance — or from particle misidentification. For instance, an electron can wrongly be identified as a photon (electron faking photon, $e \rightsquigarrow \gamma$), or an energetic neutral pion ($\pi^0 \to \gamma\gamma$) contained in a hadronic jet can wrongly be identified as a photon (jet faking photon, $j \rightsquigarrow \gamma$). Moreover, a track in a jet may also be wrongly identified as a lepton, or a lepton from a heavy-flavour quark decay may appear as an isolated lepton (jet faking lepton, $j \rightsquigarrow \ell$). Finally, events from top-quark production, with subsequent semi-leptonic $t \to W(\to \ell\nu)b$ decay, contain genuine E_T^miss, one or two leptons, and one or two b-jets that may fail a b-jet veto.

Whenever higher-order cross-section computations are available [46–48], they are used to rescale the cross-section of the generator. Finally, a specific treatment was applied to processes with possible overlaping events in $Z\gamma$ and Z+jets, VV and $VV\gamma$ or in $t\bar{t}$ and $t\bar{t}\gamma$. In order to avoid duplicated events, the overlap removal algorithm gives preference to photons produced in matrix elements (ME) over the ones from intial/final state radiations or decays. As an example, overlapping events were removed from Z+jets and kept in the $Z\gamma$ process. Finally, $\ell\ell$ final states consist of ee and $\mu^+\mu^-$ channels and include the leptonic decay of τ-leptons.

Irreducible background: These processes were generated according to the number of leptons in their final states as $\ell\ell\nu\nu\gamma$, $\ell\ell\ell\nu\gamma$ and $\ell\ell\ell\ell\gamma$ using the SHERPA v2.2.11 [49] event generator at NLO with up to three jets at the leading order (LO). In addition, contributions from off-shell bosons were also included. The full event was generated using NNPDF30_nnlo_as_0118 libraries and tuning developed by the Sherpa authors [42].

$Z\gamma$+ jets and $W\gamma$+ jets productions: The $Z(\to \ell\ell)\gamma$+ jets and $W(\to \ell\nu)\gamma$+ jets processes are split into two components based on the order in the electroweak coupling constant α_EWK. The strongly-produced component is of order α_EWK^3 and the electroweak component is of order α_EWK^5. The strong background processes of $Z(\to \ell\ell)\gamma$+ jets are modelled using filtered SHERPA 2.2.8 [37] samples. These samples are filtered by requiring a vector boson $p_\text{T} > 90$ GeV and are merged with SHERPA 2.2.8 $V\gamma$+ jets samples produced with a biased phase space enhancing $p_\text{T}(V)$ and $p_\text{T}(\gamma)$ at high values. A photon filter was applied, with $p_\text{T} > 7$ GeV, for all the merged $Z(\to \ell\ell)\gamma$+ jets samples. These calculations use the Comix [50] and Open-Loops [51] matrix element generators, and merging is done with the SHERPA parton shower [52] using the ME+PS@NLO prescription [53]. The NNPDF30_nnlo_as_0118 PDF and tuning [42] is used. Matrix elements for the strongly-produced contribution are calculated at NLO in α_s for up to two additional final-state partons, and at LO for up to three additional partons with NLO EWK+QCD corrections used as the central value for SHERPA. Matrix elements for the electroweak VBF contribution are calculated at LO in α_s with five final-state partons (e.g. $\ell^+\ell^-\gamma jj$ QCD=0) in MADGRAPH 2.6.5. The LO interference between this electroweak and strong production samples was generated, and its cross-section is about 5% of the electroweak sample. This value is taken into account as an uncertainty on the electroweak background contribution. The showering is done using PYTHIA8.240 [54] and merged in the CKKW-L scheme [55]. The photon p_T is required to be larger than 10 GeV, and the Frixione isolation [56] is applied to remove overlap with charged partons.

Z+jets production: The modelling of Z+jets is crucial in this analysis. This background has significant systematic uncertainties, as the modelling of the E_T^{miss} depends on the modelling of pile-up interactions and on the jet energy response. The Z+jets samples used are simulated using the SHERPA 2.2.1 event generator and the NNPDF3.0 NNLO libraries and the SHERPA tuning, with the invariant $\ell\ell$ mass $m_{\ell\ell} > 40$ GeV.

Top-quark pair and single top-quark productions: Background samples for top-quark pair production, as well as single top-quark, including Wt production, were simulated using POWHEG BOX v2 interfaced with PYTHIA8.230 with the NNPDF2.3LO libraries and the A14 tuning was used. Both s-channel and t-channel productions are included in the single top-quark samples. The diagram removal scheme (DR) [57] is used to remove interferences and overlap between the tW and $t\bar{t}$ productions.

$t\bar{t}$ (V, VV), $t\bar{t}\gamma$ and $Wt\gamma$ production: Background samples for top-quark pair production in association with one or two vector bosons (W or Z) or a photon, as well as single top-quark with an additional W and γ were simulated with the MADGRAPH5_aMC@NLO 2.3.3 generator [58] interfaced with PYTHIA8.210 with the NNPDF2.3LO libraries and the A14 tune.

SM Higgs boson production: Different production modes are considered as backgrounds as they can produce ffinal states with $\ell^+\ell^- + \gamma + E_T^{miss}$. Higgs bosons produced in association with a W or Z boson as well as Higgs bosons produced via gluon-gluon fusion (ggF), vector boson fusion (VBF) and ttH productions were all considered. These samples were generated using POWHEG BOX v2 with the NNPDF3.0 libraries and then showered with PYTHIA8.230 and AZNLO tuning.

Di-boson production: $ZZ \rightarrow \ell^+\ell^-\ell'^+\ell'^-$, $ZZ \rightarrow \ell^+\ell^-\nu\bar{\nu}$, $WZ \rightarrow \ell\nu\ell^+\ell^-$ and $WW \rightarrow \ell^+\nu\ell^-\bar{\nu}$ ($\ell = e, \mu$) processes are simulated using the SHERPA2.2.2 [49] event generator with NNPFD3.0NNLO libraries in the case of qq and gg-initiated production. The $gg \rightarrow ZZ$ processes include a QCD k-factor of 1.7 which was calculated from the ratio NLO/LO of the corresponding cross-sections at 13 TeV [39]. The $qq \rightarrow \ell^+\ell^-\nu\bar{\nu}$ samples include both ZZ and WW events.

Tri-boson production: The expected contribution from this background is very minor as it is suppressed by the requirement of no more than two leptons in the final state. Tri-boson production, VVV, with $V = W$ or Z, is simulated by the SHERPA2.2.2 event generator at NLO with NNPDF3.0 NNLO PDF libraires and tuning.

5 Event reconstruction and selection

5.1 Event reconstruction

Candidate events are required to have a reconstructed vertex with at least two associated tracks, originating from the beam collision region in the $x - y$ plane, with $p_T > 0.5$ GeV. The primary vertex in the event is selected as the vertex with the highest scalar sum of the squared p_T of associated tracks [59].

Electrons are reconstructed by matching clustered energy deposits in the EM calorimeters to tracks in the ID [60]. Candidates falling within the transition regions between the barrel and endcap EM calorimeters ($1.37 < |\eta| < 1.52$) are also included. All electrons must fulfill $p_T > 4.5$ GeV and $|\eta| < 2.47$ as well as loose identification criteria [60]. A longitudinal impact parameter requirement of $|z_0 \sin(\theta)| < 5$ mm as well as a transverse impact parameter satisfying $|d_0|/\sigma(d_0) < 5$ are required to ensure that electrons originate from the primary vertex.

Muons are reconstructed by matching ID tracks to MS tracks or track segments, by matching ID tracks to a calorimeter energy deposit compatible with a minimum-ionizing particle, or by identifying MS tracks passing the loose requirement and compatible with the primary vertex [61]. Muon candidates are required to fulfill $p_T > 4$ GeV, $|\eta| < 2.7$ and a very loose isolation criterion. A longitudinal impact parameter requirement of $|z_0 \sin(\theta)| < 5$ mm as well as a transverse impact parameter satisfying $|d_0|/\sigma(d_0) < 3$ are required to ensure that muons orginate from the primary vertex as well.

Photon candidates are reconstructed from clustered energy deposits in the EM calorimeter [60]. They must fulfill $p_T > 15$ GeV, $|\eta| < 2.37$ and tight identification and isolation criteria [60]. They are also required to be outside the transition region ($1.37 < |\eta| < 1.52$) between barrel and endcap EM calorimeters.

Particle flow (PFlow) jets are reconstructed using the anti-k_t algorithm [62, 63] with a radius parameter of $R = 0.4$, using charged constituents associated with the primary vertex and neutral PFlow constituents as inputs [64]. A complete energy calibration procedure, which recovers the initial parton energies after removing pile-up effects, is then applied [65]. Jet candidates are required to have $p_T > 20$ GeV and $|\eta| < 4.5$. A jet vertex tagger (JVT) discriminant [66] is used to identify jets within $|\eta| < 2.5$ originating from the hard scattered (HS) interaction through the use of tracking and vertexing. For jets with $|\eta| > 2.5$, a forward jet vertex tagging algorithm (fJVT) [67, 68] is used to reject pile-up jets. The working points used for JVT (fJVT) provide an HS selection efficiency of about 97% (93% for $p_T > 50$ GeV). In the case of b-jets, a multivariate discriminant output is used for the identification [69]. The used working point provides a 77% b-jet tagging efficiency in simulated inclusive $t\bar{t}$ events, with rejection factors of 6 and 134 for charm-hadron jets and light-flavour quark- or gluon-initiated jets, respectively.

The missing transverse momentum $\vec{E}_T^{\text{miss}}$, originating from the unbalanced momentum in the transverse plane, is defined as the negative vectorial sum of the transverse momenta of all selected (hard objects) electrons, muons, photons, PFlow jets, as well as the "soft term", which is estimated from tracks compatible with the primary vertex, but not matched to any of those objects [70]. Jets are only included in the $\vec{E}_T^{\text{miss}}$ definition if they have $p_T > 20$ GeV and satisfy the tight JVT and fJVT selections in order to mitigate pile-up effects. Moreover, an E_T^{miss} significance S is defined to reduce the effects on E_T^{miss} from resolution fluctuations. S is a powerful quantity to discriminate between events with fake $\vec{E}_T^{\text{miss}}$, arising from instrumental sources or poorly reconstructed physics objects and events with genuine $\vec{E}_T^{\text{miss}}$ originating from weakly interacting particles, like neutrinos. The variable S is calculated as $|\vec{E}_T^{\text{miss}}|/\left[\sigma_L^2 \left(1 - \rho_{LT}^2\right)\right]^{1/2}$, where σ_L is the total standard deviation in the direction longitudinal to the $\vec{E}_T^{\text{miss}}$ corresponding to the summation of the covariance matrices from resolution effects of physics objects and soft term entering the $\vec{E}_T^{\text{miss}}$ calculation and ρ_{LT} is the correlation factor of the longitudinal (L) and transverse (T) measurements [71].

To resolve ambiguities in the reconstruction of physics objetcs and to avoid double counting of energy deposits and momentum measurements, a ΔR separation is required as detailed in Table 2.

Finally, several cleaning requirements are applied to suppress non-collision backgrounds [72]. Misreconstructed (bad quality) jets can be caused by electronic noise, and jets from collisions are identified by

Table 2: Overview of the overlap removal between reconstructed physics objects and the corresponding matching criteria in order of priority.

Remove	Keep	Matching criteria
jet	electron	$\Delta R < 0.2$
jet	muon	number of tracks < 3 and $\Delta R < 0.2$
jet	photon	$\Delta R < 0.4$
electron	jet	$0.2 < \Delta R < 0.4$
electron	muon	shared same ID track
electron	electron	shared same ID track, electron with lower p_T removed
muon	jet	$0.2 < \Delta R < 0.4$
muon	electron	muon with calorimeter deposits and shared ID track
photon	electron	$\Delta R < 0.4$
photon	muon	$\Delta R < 0.4$

requiring a good fit to the expected pulse shape for each constituent calorimeter cell. Cosmic-ray showers and beam-halo interactions with the LHC collimators are another source of misreconstructed jets. Those jets are identified by requirements on their energy distribution in the calorimeter and the fraction of their constituent tracks that originate from the primary vertex. Events are rejected if they contain a bad quality jet with $p_\mathrm{T} > 20$ GeV as they tend to give rise to fake $E_\mathrm{T}^\mathrm{miss}$ and a poor description of its distribution in the tail region.

5.2 Signal region selection

The signal region (SR) targets the $\ell^+\ell^-+\gamma+E_\mathrm{T}^\mathrm{miss}$ final state, where the two same-flavour, oppositely charged leptons come from a Z boson decay, the photon comes from the Higgs boson decay and the $E_\mathrm{T}^\mathrm{miss}$ arises from the potential undetected dark photon. Accepted leptons are required to match the corresponding online trigger candidates, and trigger scale factors and their uncertainties are applied. Table 3 lists the event selections in the SR, optimised using a multivariate approach to maximize the signal over background acceptance. A BR($H \rightarrow \gamma\gamma_d$) = 5% was assumed for all dark photon masses. The resulting acceptance times efficiency for combined $qqZH$ and $ggZH$ signal events amounts to 10.5% for all considered γ_d masses.

Accepted signal electrons, reconstructed using a likelihood-based identification algorithm, must fulfill a 'Medium' criteria [60], while 'Loose' criteria are used to veto additional electrons in the SR. The likelihood relies on the shape of the EM shower measured in the calorimeter, the quality of the track reconstruction, and the quality of the match between the track and the cluster. Similarly, selected muons are also required to have 'Medium' quality identification [61] while 'Loose' criteria are used to veto additional muons. To suppress hadronic and non-prompt lepton backgrounds, electron and muon candidates are required to satisfy the particle-flow 'Loose' isolation criteria, which are based on tracking and calorimeter measurements [61]. The veto on events with a third loose lepton is used to reduce $ZZ \rightarrow \ell^+\ell^-\ell'^+\ell'^-$ and $WZ \rightarrow \ell\nu\ell^+\ell^-$ contributions. The invariant mass of the selected lepton pairs $m_{\ell\ell}$ is required to be within the Z boson peak ([76 − 116] GeV) to reject processes such as $t\bar{t}$ and $WW \rightarrow \ell^+\nu\ell^-\bar{\nu}$.

Exactly one 'Tight' photon, satisfying the tight isolation criteria [60] is required. The isolation section requires that the sum of the transverse energies (at the electromagnetic scale) of positive-energy topological

Table 3: Optimised kinematic selections defining the signal region for $\ell^+\ell^- + \gamma + E_{\mathrm{T}}^{\mathrm{miss}}$.

Two same flavour, opposite sign, medium ID and loose isolated leptons, with leading $p_{\mathrm{T}} > 27$ GeV, sub-leading $p_{\mathrm{T}} > 20$ GeV
Veto events with additional lepton(s) with loose ID and $p_{\mathrm{T}} > 10$ GeV
76 GeV $< m_{\ell\ell} < 116$ GeV
Only one tight ID, tight isolation photon with $E_{\mathrm{T}}^{\gamma} > 25$ GeV
$E_{\mathrm{T}}^{\mathrm{miss}} > 60$ GeV with $\Delta\phi(\vec{E}_{\mathrm{T}}^{\mathrm{miss}}, \vec{p}_{\mathrm{T}}^{\ell\ell\gamma}) > 2.4$ rad
$m_{\ell\ell\gamma} > 100$ GeV
$\mathrm{N_{jet}} \leq 2$, with $p_{\mathrm{T}}^{\mathrm{jet}} > 30$ GeV, $|\eta| < 4.5$
Veto events with b-jet(s)

clusters located within a distance $\Delta R = 0.4$ of the photon candidate γ must be less than $0.22 \times E_{\mathrm{T}}^{\gamma} + 2.45$ [GeV], where E_{T}^{γ} is the transverse energy of the photon. In addition, the scalar sum of the p_{T} of all tracks located within a distance $\Delta R = 0.2$ of the photon candidate must be less than $0.05 \times E_{\mathrm{T}}^{\gamma}$ [GeV].

Other selections are applied, which exploit the topology and kinematics of the signal events. A threshold on $E_{\mathrm{T}}^{\mathrm{miss}}$ was optimised to select signal events while rejecting the inclusive Z production. In addition, $\vec{E}_{\mathrm{T}}^{\mathrm{miss}}$ is expected to be back-to-back with the $(Z - \gamma)$ system, leading to a requirement on the azimuthal separation $\Delta\phi(\vec{E}_{\mathrm{T}}^{\mathrm{miss}}, \vec{p}_{\mathrm{T}}^{\ell\ell\gamma})$ applied in the SR. Furthermore, events with more than 2 jets (with $p_{\mathrm{T}}^{\mathrm{jet}} > 30$ GeV, $|\eta| < 4.5$) are rejected to reduce contributions from V+jets processes. Finally, a veto on any b-tagged jet is also applied to reduce processes with a top quark.

Events are categorised into two sub-regions called, respectively, e^+e^-- and $\mu^+\mu^-$-channel. The expected signal and background composition in each SR, as predicted from MC simulation, after all the optimisations, is shown in Table 4. It should be noticed that the VV background is dominated by the WZ process where the photon is the result of an electron mis-identification while contributions from WW, ZZ are found to be negligible due to the very low probability of jets to be mis-identified as photons. The $VV\gamma$ background is dominated by $ZZ\gamma$ and $WW\gamma$ contributions from the $\ell\ell\nu\nu\gamma$ final state.

Table 4: Expected event yields for signal and background in the SR corresponding to $\mathcal{L} = 139$ fb^{-1}. Signal events are for massless γ_d, assuming BR($H \to \gamma\gamma_d$) = 5%. Events for background processes are categorised as $Z\gamma$ (QCD+EWK $Z\gamma$), Z+jets (QCD+EWK Z+jets), Top (single top-quark, Wt), $t\bar{t}$ ($t\bar{t}, t\bar{t}V, t\bar{t}VV$), Top$\gamma$ ($Wt\gamma$), $VV\gamma$ ($WW\gamma, WZ\gamma, ZZ\gamma$), VV (WW, WZ, ZZ), SM Higgs (ggH, VH, VBF H) and $W\gamma$ (QCD+EWK $W\gamma$). Only statistical uncertainties on the simulated samples are shown.

Channel	Signal	$Z\gamma$	Z+jets	Top	$t\bar{t}$	Topγ	$VV\gamma$	VV	SM Higgs	$W\gamma$	Total background
ee	19.3 ± 0.2	155 ± 15	274 ± 55	3.5 ± 0.7	25 ± 1	1.9 ± 0.1	26 ± 1	27 ± 1	0.41 ± 0.01	3.5 ± 1.5	517 ± 57
$\mu\mu$	22.4 ± 0.2	283 ± 18	380 ± 63	4.6 ± 0.8	26 ± 1	2.4 ± 0.1	35 ± 1	24 ± 1	0.54 ± 0.01	1.6 ± 1.1	758 ± 66

In order to enhance the sensitivity of the search for the γ_d signal, a boosted decision tree (BDT) algorithm was implemented using the XGBoost classifier [73]. For training and testing, all events entering the SR are used. All signal events are assigned to the positive class (y = 1) and all background events are assigned to the negative class (y = 0) in the training data. The model has been trained using a feature set consisting of the following 6 variables, according to their ranking: S (E_T^{miss} significance), m_T (Equation 1), $m_{\ell\ell}$, p_T^γ, $m_{\ell\ell\gamma}$, and p_T^{ratio} (Equation 2), with:

$$m_T = \sqrt{2E_T^{miss} p_T^\gamma [1 - \cos[\Delta\phi(\vec{E}_T^{miss}, \vec{p}_T^\gamma)]]} \tag{1}$$

$$p_T^{ratio} = \frac{|\vec{E}_T^{miss} + \vec{p}_T^\gamma| - p_T^{\ell\ell}}{p_T^{\ell\ell}} \tag{2}$$

To train the BDT, the simulated samples introduced in section 4 for the signal and the background processes are used. The signal samples for all considered γ_d masses were merged and the same weight was assigned to their events. To enhance the statistical power of the training sample, a five-fold cross validation strategy was adopted. The simulation samples were divided into five equal subsets. Five BDT classifiers with the same input variables were trained. In each BDT training, four subsets of simulation samples were used as the training sample, and the remaining subset was used as the testing sample. The five BDT trainings correspond to the five possible permutations of such training-testing setups. The five trained BDT models were used to calculate the BDT score of data that were divided into five subsets in the same manner. The BDT classifier output is then used as an observable for the final statistical analysis as discussed in Section 8.

6 Treatment of the background processes

The different background sources, described in Section 4.2, are classified into disjoint categories, described below, according to their treatment in the analysis. In what follows, weak bosons W, Z are always meant to decay leptonically: $W \to \ell\nu$ and $Z \to \ell^+\ell^-$, unless stated otherwise.

- **Irreducible background from $VV\gamma$ final states**: $Z(\to \ell^+\ell^-)Z(\to \nu\bar{\nu})\gamma$ and $W^+(\to \ell^+\nu)W^-(\to \ell^-\bar{\nu})\gamma$.

- **Background from electrons faking photons** ($e \rightsquigarrow \gamma$): the involved final states are mostly $Z(\to \ell^+\ell^-)W(\to e\nu)$, and to a lesser extent also $Z(\to \ell^+\ell^-)Z(\to e^+e^-)$ with an undetected electron, VVV with undetected leptons, and finally $\ell^+\ell^-Vt$ and $VVt\bar{t}$ that were not rejected by the b-veto.

- **Background from fake E_T^{miss}**: the largest contribution comes from $Z\gamma$ + jets and Z + jets, where the E_T^{miss} mismeasurement is mostly due to jet energy mismeasurement. In order for the Z + jets to mimic the signal sought, one jet must be misreconstructed as a photon; this source of background is therefore included in the fake E_T^{miss} estimation. Minor contributions to this category come from $Z\gamma\gamma$ and $ZH(\to \gamma\gamma)$ with an undetected photon, and from $gg \to H$ and VBF Higgs production with subsequent $H \to Z\gamma$ decay. The ZZ and VVV final states are not included in this category, as they are already accounted for in the $e \rightsquigarrow \gamma$ case.

- **Background from top quark production**: the main final states are $tW\gamma$, $t\bar{t}\gamma$, $t\bar{t}$ and single top-quark production — in the last two cases, the identified photon comes from $j \rightsquigarrow \gamma$. The $\ell^+\ell^- Vt$ and $VVt\bar{t}$ events are not included in this category, as they already enter the $e \rightsquigarrow \gamma$ category.

- **Background from $W\gamma$**: enters the SR due to a jet faking a lepton.

- **Other background from Higgs: $t\bar{t}H(\rightarrow Z\gamma)$ and $VH(\rightarrow Z\gamma)$**: this category can be divided into $t\bar{t}H(\rightarrow Z\gamma)$, $ZH(\rightarrow Z\gamma)$ and $W(\rightarrow \ell\nu)H(\rightarrow Z\gamma)$. Their experimental effects differ: the first one fails the b-veto; the second is irreducible, if one of the two Zs decays to $\nu\bar{\nu}$ and the other to $\ell^+\ell^-$; the third has genuine $E_{\mathrm{T}}^{\mathrm{miss}}$ and an undetected lepton. However, their contributions are so tiny (by 3 or 4 orders of magnitude) with respect to any other concurrent process that it is more convenient to treat them all in a dedicated category. Note that this category does not include all processes involving the Higgs boson, as some are already accounted for in previously described categories.

The background contributions coming from the fake $E_{\mathrm{T}}^{\mathrm{miss}}$ category (which is dominant) and from the $e \rightsquigarrow \gamma$ category are estimated with data-driven techniques. The other categories are estimated from MC simulation. The normalization for the top-quark background is checked in a dedicated validation region (VR), while the normalization of $VV\gamma$ irreducible background is adjusted in a dedicated control region (CR), as described in Section 6.3.

6.1 Evaluation of the background from electrons faking photons

This background occurs because electrons and photons produce similar shower shapes in the EM calorimeter, and photons may convert early in the tracker into an asymmetric e^+e^- pair where one track may not be reconstructed; to keep the photon detection efficient, such cases must be considered, at the price of having a background from electrons wrongly identified as photons.

As this background cannot be perfectly modeled in simulation, a two step data-driven approach has been performed. First, the "electron-to-photon fake rate", $f_{e\rightsquigarrow\gamma}$ is estimated. This rate is then applied to a "probe-electron" CR, whose events are selected with the same criteria as for the SR, but requiring an extra electron instead of the photon — called "probe electron", e_p, in the following.

To estimate $f_{e\rightsquigarrow\gamma}$, two set of data events are selected, respectively with e^+e^- and $e^\pm\gamma$ final states, with no additional leptons or photons. The distributions of the invariant masses, m_{ee} and $m_{e\gamma}$, for the two final states, both exhibit a peak around the Z mass, on top of a continuous background. The Z contribution is extracted by means of a functional fit, where the peak is modeled as a double-sided Crystal Ball function, while the continuum is described by an exponential of a polynomial function. The quantity $f_{e\rightsquigarrow\gamma}$ is computed from the results of this fit as the ratio of the number of events from $Z \rightarrow e^+e^-$ and from $Z \rightsquigarrow e^\pm\gamma$ where the second category counts the $e^\pm\gamma$ mis-identification.

The estimate is done in several bins of photon p_{T} and η, as $f_{e\rightsquigarrow\gamma}$ exhibits a strong dependance on these two variables. The values of $f_{e\rightsquigarrow\gamma}$ increase both as a function of η and p_{T}, ranging from 1.3–3% in the barrel, to about 7% at high p_{T} in the endcap. The overall uncertainty on each value is evaluated combining in quadrature the statistical uncertainties of the data samples, a systematic uncertainty quantifying the deviation between the actual and fitted peak, and an additional systematic uncertainty from a non-closure of the whole procedure carried out on MC simulation. The overall relative uncertainty on $f_{e\rightsquigarrow\gamma}$ ranges from 7% to 11%.

The probe-electron CR (e_p-CR) is populated with $\ell^+\ell^- e_p + E_T^{\text{miss}}$ events, where the probe electron must satisfy the same kinematic requirements as the photon: in particular $p_T^{e_p} > 25$ GeV, $|\eta^{e_p}| < 1.37$ or $|\eta^{e_p}| \in [1.52, 2.37]$, $m_{\ell\ell e_p} > 100$ GeV, and $\Delta\phi(\vec{E}_T^{\text{miss}}, \vec{p}_T^{\ell\ell e_p}) > 2.4$ rad. The rest of the event satisfies the same requirements as for the SR. Each event in the e_p-CR is then scaled by the respective $f_{e\rightsquigarrow\gamma}$, computed as a function of η^{e_p} and $p_T^{e_p}$; the number of the scaled events gives the estimate of the $e \rightsquigarrow \gamma$ background in the SR. Since this procedure is done per-event, it also allows for the estimation of the distributions of all kinematic variables for this background.

For the $\mu^+\mu^-$ channel and the e^+e^- channel the final states of the e_p-CRs are respectively $\mu^+\mu^- e_p + E_T^{\text{miss}}$ and $e^+e^- e_p + E_T^{\text{miss}}$; in the latter case, there is an ambiguity about which of the three electrons to be considered as the e_p. In principle, any of the three could be mis-identified as a photon; however, the opposite-charge requirement on the remaining e^+e^- pair always rules out one of the 3 possibilities.

In the e_p-CR, there is a contamination of jets faking electrons, occurring at a rate $f_{j\rightsquigarrow e}$, which is estimated from simulation at the level of 6%–7%. This is accounted for by rescaling all events in the e_p-CR by a quantity $1 - f_{j\rightsquigarrow e}$; a systematic uncertainty equal to $f_{j\rightsquigarrow e}$ is assigned to this correction.

The data-driven estimates of the background from $e \rightsquigarrow \gamma$ in the e^+e^- channel and $\mu^+\mu^-$ channel are, respectively, 21.0 ± 2.4 and 20.4 ± 2.1 events. The errors are evaluated combining in quadrature the statistical uncertainty of the e_p-CR, the uncertainty on $f_{e\rightsquigarrow\gamma}$ and on $f_{j\rightsquigarrow e}$.

6.2 Evaluation of the background from fake E_T^{miss}

The data-driven estimate of the background from fake E_T^{miss} is achieved by means of an "ABCD method"; besides the SR (here labelled region A), three CRs (B, C, D) are defined by inverting the selection cuts on the E_T^{miss} and $\Delta\phi(\vec{E}_T^{\text{miss}}, \vec{p}_T^{\ell\ell\gamma})$ variables:

- **region A**: $E_T^{\text{miss}} > 60$ GeV and $\Delta\phi(\vec{E}_T^{\text{miss}}, \vec{p}_T^{\ell\ell\gamma}) > 2.4$ rad;

- **region B**: $E_T^{\text{miss}} \in [30, 40]$ GeV and $\Delta\phi(\vec{E}_T^{\text{miss}}, \vec{p}_T^{\ell\ell\gamma}) > 2.4$ rad;

- **region C**: $E_T^{\text{miss}} > 60$ GeV and $\Delta\phi(\vec{E}_T^{\text{miss}}, \vec{p}_T^{\ell\ell\gamma}) < 2.4$ rad;

- **region D**: $E_T^{\text{miss}} \in [30, 40]$ GeV and $\Delta\phi(\vec{E}_T^{\text{miss}}, \vec{p}_T^{\ell\ell\gamma}) < 2.4$ rad.

Two more validation regions (VR) are introduced:

- **region A'**: $E_T^{\text{miss}} \in [40, 60]$ GeV and $\Delta\phi(\vec{E}_T^{\text{miss}}, \vec{p}_T^{\ell\ell\gamma}) > 2.4$ rad;

- **region C'**: $E_T^{\text{miss}} \in [40, 60]$ GeV and $\Delta\phi(\vec{E}_T^{\text{miss}}, \vec{p}_T^{\ell\ell\gamma}) < 2.4$ rad.

as illustrated in Figure 2.

The regions B, C, D are built such as to be enriched in events with fake E_T^{miss}. The residual contribution of events with genuine E_T^{miss} is subtracted; a large portion of them come from the $e \rightsquigarrow \gamma$ background, and therefore can be evaluated and subtracted by applying the data-driven procedure described in Section 6.1 to
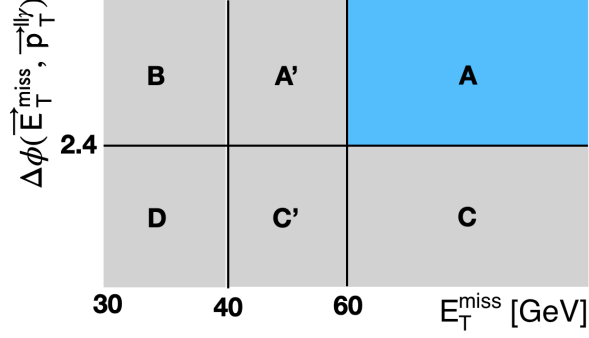
Figure 2: Regions involved in the "ABCD" method for estimation of the background from fake $E_{\mathrm{T}}^{\mathrm{miss}}$; region A is the signal region.

the specific regions. The other processes ($VV\gamma$, top, $W\gamma$, and $t\bar{t}H + VH$) are estimated from simulation and subtracted. Then, the fake $E_{\mathrm{T}}^{\mathrm{miss}}$ background in region A can be computed as:

$$N_A^{\text{fake } E_{\mathrm{T}}^{\mathrm{miss}}} = R \cdot \frac{N_B^{\text{fake } E_{\mathrm{T}}^{\mathrm{miss}}} \cdot N_C^{\text{fake } E_{\mathrm{T}}^{\mathrm{miss}}}}{N_D^{\text{fake } E_{\mathrm{T}}^{\mathrm{miss}}}} \tag{3}$$

where R is a parameter that accounts for the correlation between the variables $E_{\mathrm{T}}^{\mathrm{miss}}$ and $\Delta\phi(\vec{E}_{\mathrm{T}}^{\mathrm{miss}}, \vec{p}_{\mathrm{T}}^{\ell\ell\gamma})$ in the fake $E_{\mathrm{T}}^{\mathrm{miss}}$ processes — if the two variables were independent, $R = 1$. The variables were chosen so as to have R close to 1 and to be stable when varying the requirements on each of the variables used.

The value of R is estimated from MC simulation; the dominant processes to the fake $E_{\mathrm{T}}^{\mathrm{miss}}$ background are $Z\gamma$ + jets and Z + jets. In these processes, only few events enter the A, C regions, causing the statistical uncertainty on R to be large; to overcome this, regions ($A + A'$) and ($C + C'$) are used instead, exploiting the stability of R with respect to the value of the $E_{\mathrm{T}}^{\mathrm{miss}}$ cut. Moreover, the compatibility of the R-value obtained with this approach with that from A, C regions has been checked. The extracted value for:

$$R_{\mathrm{MC}} = \frac{N_{A+A'}^{Z(\gamma)+\text{jets}} \cdot N_D^{Z(\gamma)+\text{jets}}}{N_B^{Z(\gamma)+\text{jets}} \cdot N_{C+C'}^{Z(\gamma)+\text{jets}}} \tag{4}$$

is displayed in Table 5, for the ee and $\mu\mu$ channels; the quoted uncertainties are due to the statistical uncertainties on the MC simulation. The relative contribution of $Z\gamma$ + jets and Z + jets processes, and the $j \rightsquigarrow \gamma$ fake rate occurring in the second case, are known not to be precisely modeled by MC simulation; for this reason, the contribution of the Z + jets process has been changed by $\pm 50\%$ of the MC prediction, to check its impact on R_{MC}. The result is also shown in Table 5; the small variations are well covered by the statistical uncertainties, therefore there is no evidence that the amount of Z + jets has an impact on R_{MC}.

A further check on the reliability of R_{MC} has been carried out exploiting the two VRs A', C', where a similar factor:

$$R' = \frac{N_{A'}^{\text{fake } E_{\mathrm{T}}^{\mathrm{miss}}} \cdot N_D^{\text{fake } E_{\mathrm{T}}^{\mathrm{miss}}}}{N_B^{\text{fake } E_{\mathrm{T}}^{\mathrm{miss}}} \cdot N_{C'}^{\text{fake } E_{\mathrm{T}}^{\mathrm{miss}}}} \tag{5}$$

16

is introduced, and computed from MC simulation and data. R'_{MC} is computed using $Z\gamma$ + jets and Z + jets processes, while R'_{data} uses event counts after the subtraction of $e \rightsquigarrow \gamma$, $VV\gamma$, top, $W\gamma$ and VH background processes. The results are shown in Table 5; the comparison of R'_{MC} and R'_{data} shows no significant discrepancy. As a conclusion, the evaluation of R_{MC} is considered reliable, and is used in Equation (3).

Table 5: Values of R for the ee and $\mu\mu$ channels. R_{MC} is computed from simulation, assuming a relative amount of Z + jets with respect to $Z\gamma$ + jets processes as predicted by the simulation (nominal), or changed by factors 0.5 or 1.5. R' is computed using regions A', C' instead of $(A + A')$ and $(C + C')$, to allow a comparison between simulation and data in a sample enriched by fake E_T^{miss}. Statistical uncertainties on the simulated samples are reported.

| channel | R_{MC} | | | R' | |
	nominal	$0.5 \times (Z + \text{jets})$	$1.5 \times (Z + \text{jets})$	R'_{MC}	R'_{data}
ee	1.12 ± 0.11	1.15 ± 0.13	1.06 ± 0.08	1.09 ± 0.11	1.16 ± 0.06
$\mu\mu$	1.24 ± 0.11	1.25 ± 0.14	1.23 ± 0.09	1.15 ± 0.11	1.18 ± 0.05

The data-driven estimates of the fake E_T^{miss} background in the ee and $\mu\mu$ channels are, respectively, 413 ± 50 and 581 ± 64 events. The errors are evaluated from the propagation of the statistical uncertainties of R_{MC} and of data in the ABCD regions.

6.3 Treatment of the irreducible background and the top-quark background

The irreducible $VV\gamma$ background plays an important role at high values of the BDT score, which drive the sensitivity of the search; for this reason, a dedicated "$VV\gamma$-CR" is introduced, to correct the normalisation of this background (see Section 8). Recalling that such a background is a pure electroweak process, to which $Z(\rightarrow \ell^+\ell^-)Z(\rightarrow \nu\bar{\nu})\gamma$ and $W^+(\rightarrow \ell^+\nu)W^-(\rightarrow \ell^-\bar{\nu})\gamma$ contribute, the "$VV\gamma$-CR" has been built to be enriched in $Z(\rightarrow \mu^+\mu^-)W(\rightarrow \mu\nu)\gamma$, thus requiring exactly three muons, one photon and no electrons. The opposite-charge $\mu^+\mu^-$-pair whose invariant mass is closest to the Z mass must fulfil all $\ell^+\ell^-$ kinematic cuts of the SR; to reduce the statistical uncertainty, no requirements are applied on E_T^{miss} and $\Delta\phi(\vec{E}_T^{miss}, \vec{p}_T^{\ell\ell\gamma})$. The purity of $ZW\gamma$ events in such a CR is estimated to be 83% from simulation.

To check the normalization of the top-induced background predicted by simulation, a "top-VR" has been used, enriched by such processes; it is defined starting from the selection of the SR, removing the requirements on $m_{\ell\ell}$ and $\Delta\phi(\vec{E}_T^{miss}, \vec{p}_T^{\ell\ell\gamma})$, and requiring at least one b-tagged jet. The purity of events with top-quark production is estimated to be 92% from simulation in such a VR.

6.4 Background checks in validation region

As an overall check of the background estimates, the data-driven techniques described in Section 6.2 and Section 6.1 are applied in the VR A' (Figure 2). The comparison between the expected background and data is displayed in Figures 3 and 4, showing good agreement.

7 Systematic uncertainties

This section presents the various sources of systematic uncertainties affecting all levels of the analysis. They are categorised according to their origin, effects and the way they have been estimated.
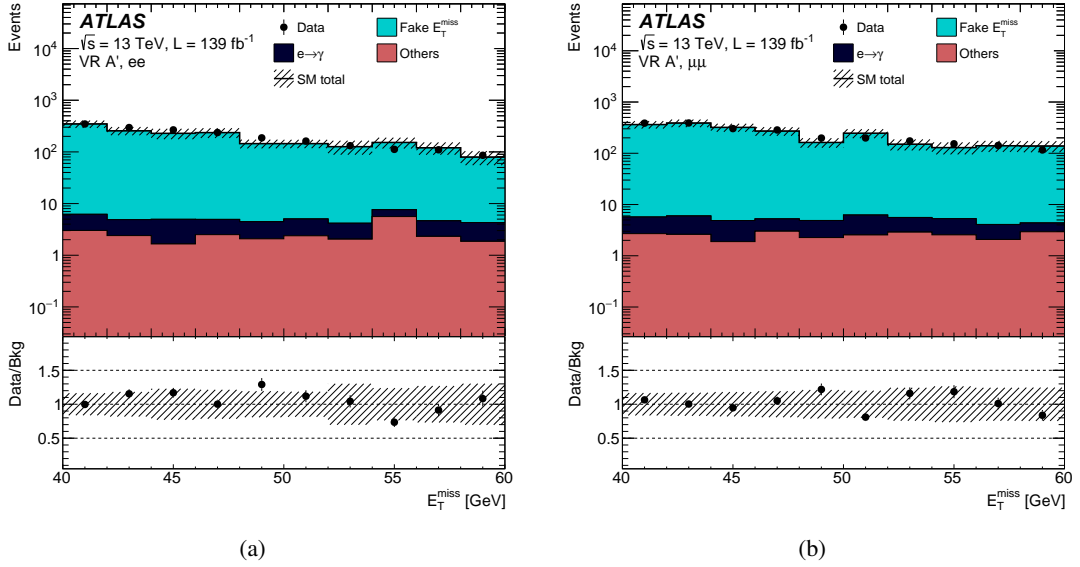
Figure 3: Comparison between the expected background and data in the validation region A', as a function of E_T^{miss}, for the ee (a) and $\mu\mu$ (b) channels. The background yields from "fake E_T^{miss}" and "$e \rightsquigarrow \gamma$" are estimated with data-driven techniques. The other backgrounds are obtained from simulation and have been merged together. Uncertainties shown are statistical, both for data and for simulated backgrounds, while for the data-driven backgrounds the systematic uncertainties related to the method are also included.

7.1 Experimental systematic uncertainties

The analysis is impacted by several uncertainties related to the detector resolution, inefficiencies and mis-measurements. They are grouped into the following categories: uncertainties in the luminosity, uncertainties in the trigger efficiencies and uncertainties related to the reconstruction of physics objects such as electrons, muons, jets, and E_T^{miss}. The estimations of these uncertainties require a particular treatment as they affect the search via potential biases to the modelling of the signal and background processes in the MC simulation. These systematic uncertainties can affect both the yield and the shape of the final observable (BDT classifier response) and are included in the statistical evaluation.

The uncertainty in the luminosity is 1.7% [74] and impacts the simulated yields of both the signal and backgrounds. This uncertainty was obtained using the LUCID-2 detector [75] for the primary luminosity measurements. In addition, systematic uncertainties resulting from effects of pile-up modeling, due to the reweighting procedure, are also considered.

Systematic uncertainties are estimated for lepton reconstruction and isolation efficiencies [60, 61] and for the energy scale and resolution [60]. Additional uncertainties on lepton trigger efficiencies are also considered to take into account differences between data and simulation [29, 30].

For the photons, uncertainties in the reconstruction, isolation, energy scale and resolution are considered [60, 76].

For jets, uncertainties related to the energy and resolution [65] as well as pile-up jet tagging [77] are all taken into account. Specific systematic uncertainties are considered for heavy flavour tagging to correct for identification efficiencies of bottom, charm and light tagged jets [78, 79].
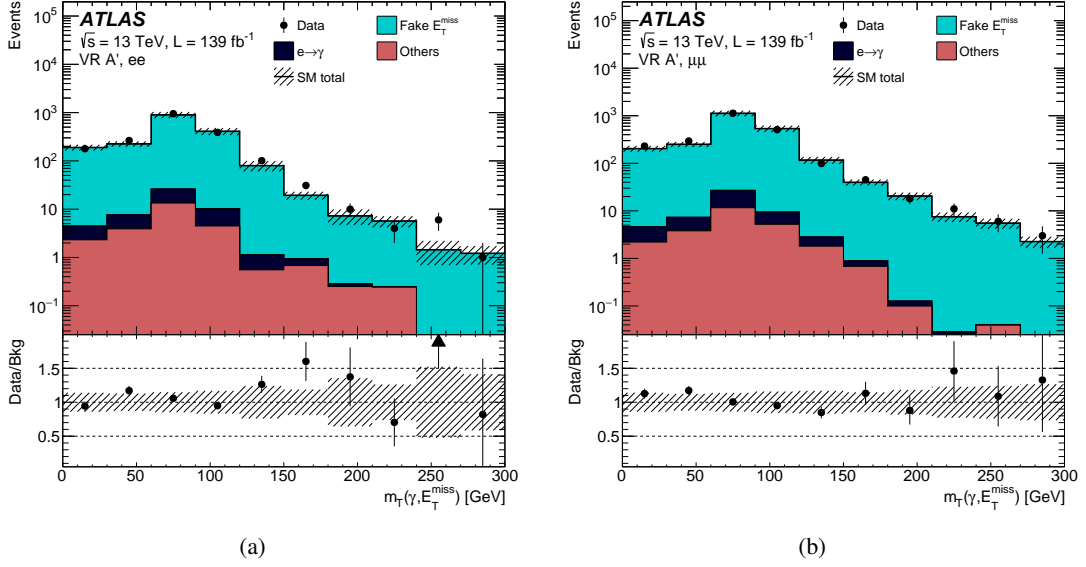
Figure 4: Comparison between the expected background and data in the validation region A', as a function of m_T, for the ee (a) and $\mu\mu$ (b) channels. The background yields from "fake E_T^{miss}" and "$e \rightsquigarrow \gamma$" are estimated with data-driven techniques. The other backgrounds are obtained from simulation and have been merged together. Uncertainties shown are statistical, both for data and for simulated backgrounds, while for the data-driven backgrounds the systematic uncertainties related to the method are also included.

For E_T^{miss}, uncertainties associated with reconstructed objects are propagated and included in its calculation. Additional uncertainties associated to the E_T^{miss} soft term scale and resolution are independently evaluated [70].

An additional uncertainty on the shape of the BDT classifier response for the fake E_T^{miss}-induced background (Section 6) is considered. It is meant to account for inaccuracies in the shape of the Z+jets MC events characterized by high bin-to-bin fluctuations. To reduce these fluctuations a Gaussian smoothing algorithm is applied to the Z+jets distribution and the uncertainty is obtained from the difference between this varied shape and the one corresponding to the nominal Z+jets MC distribution together with the other MC simulated processes entering the fake E_T^{miss} category.

Finally, the comparison between data and MC predictions in the "top-VR" shows a discrepancy at the level of 20% for top-induced background (Section 6.3). For this reason, in the treatment of such a background, a relative systematic uncertainty of ±20% is considered.

7.2 Theoretical systematic uncertainties

Theoretical uncertainties affect all simulated signal and background processes. They originate from the limited order in α_s or α_{EWK} at which the matrix elements are calculated, the matching of those calculations to parton showers and the uncertainty of the proton PDFs. The uncertainties from the variation of QCD scale and the variation of PDFs are considered for the signal and simulated background processes. Uncertainties for backgrounds entering different control (CR) and validation (VR) regions were also estimated.

For the $H \to \gamma\gamma_d$ signal, the total ZH cross-section is calculated up to NLO precision and is provided by the LHC Higgs Cross-Section Working Group [39]. NLO electroweak corrections reduce the cross section by 5.3%.

This correction has been propagated to the BDT classifier response. The corresponding systematic uncertainties are extracted from the maximum and minimum variations of the NLO corrections and amount to 0.2-0.3%. The parton shower (PS) model effects on signal processes were estimated through a comparison between PYTHIA8 and HERWIG7 showering models. The difference between the two algorithms in each BDT classifier response bin is taken as a systematic uncertainty on the PS model and amounts to 0.4-6.0% (0.2-36%) for $qq \to ZH$ ($gg \to ZH$).

For the QCD renormalisation μ_R and factorisation μ_F scales a seven-point scale variation is considered, which amounts to varying the renormalisation and factorisation scales independently by factor of 1/2 and 2 around μ to the combinations of $(\mu_R, \mu_F) = (\mu/2, \mu/2), (2\mu, 2\mu), (\mu, 2\mu), (2\mu, \mu), (\mu, \mu/2)$ and $(\mu/2, \mu)$. The effect of these variations was propagated to the BDT classifier distributions. An envelope covering differences with respect to the nominal values is taken as the systematic uncertainty.

Depending on the γ_d mass and the BDT bin, the uncertainties from PS vary from [-4,+5]% ($qqZH$) to [-19,+25]% ($ggZH$). Finally, uncertainties related to the choice of the PDF are computed by considering the yield predictions with full ensemble of 100 PDFs within the NNPDF set. The standard deviation of this set of yields is taken as the corresponding PDF uncertainty. The uncertainties related to the α_s variations are computed by considering the difference in the yield from two α_s variations (0.1195 and 0.1165). The α_s and PDF uncertainties are quadratically added and their impact varies from ±0.4% to ±1.1%.

Similar approaches have also been applied to estimate theoretical uncertainties for background processes that were evaluated using MC predictions. Up and down variations with respect to nominal values for QCD (μ_R, μ_F) scales, PDF+α_s and PS algorithms were considered as systematic uncertainties for $VH, t\bar{t}H(H \to Z\gamma), t\bar{t}, t\bar{t}V, Wt\gamma$, single top-quark, $W\gamma^{QCD,EWK}$ and $VV\gamma$. Uncertainties from PDF+α_s amount to a maximum up to ±10% ($W\gamma$, single top-quark), QCD scale up to ±30% ($t\bar{t}V$) and PS up to ±40% ($W\gamma, t\bar{t}$). Finally, theoretical uncertainties associated with $Z\gamma$ and Z+jets were also evaluated as contributions from these processes need to be known in data-driven background estimation.

8 Results and Interpretation

To estimate the compatibility of the data with the SM expectations, as well as to extract upper limits at 95% confidence level (CL) on the branching ratio of $H \to \gamma\gamma_d$ a binned maximum likelihood fit is performed in the SR to the distribution of the BDT classifier response merging the ee and $\mu\mu$ channels to obtain the best sensitivity.

The chosen binning in the SR is optimised to obtain the best expected sensitivity to the signal model, while also keeping low statistical uncertainties in each bin.

The likelihood function is built as a product of Poisson probability functions based on the expected signal and background yields in each BDT bin of the SR and in the single-bin $VV\gamma$ CR. Two free parameters are included in the simultaneous likelihood fit: the branching ratio BR($H \to \gamma\gamma_d$), which consists in the parameter of interest (POI) and multiplies the signal yield and the floating normalization factor for the $VV\gamma$ irreducible background $k_{VV\gamma}$, which is constrained by the $VV\gamma$ CR. The systematic uncertainties are

Table 6: Observed event yields in 139 fb^{-1} of data compared to expected yields from SM backgrounds obtained from the background-only fit for the $ee + \mu\mu$ channel in the SR and in the $VV\gamma$ CR. The total expected yields before the fit are also shown. The expected yields for the massless γ_d signal are shown assuming BR($H \to \gamma\gamma_d$) = 5%. The uncertainty includes both the statistical and systematic sources. The individual uncertainties can be correlated and do not necessarily add in quadrature to equal the total background uncertainty.

BDT bin	SR 0 - 0.50	SR 0.50 - 0.64	SR 0.64 - 0.77	SR 0.77 - 0.88	SR 0.88 - 0.96	SR 0.96 - 1	$VV\gamma$ CR
Observed	910	84	59	72	42	6	32
Post-fit SM background	910 ± 29	85.5 ± 8.7	59.9 ± 7.3	69.7 ± 7.8	41.6 ± 6.1	7.3 ± 2.0	31.4 ± 5.4
Fake E_T^{miss}	800 ± 34	72.1 ± 8.3	45.7 ± 6.5	53.2 ± 7.1	27.9 ± 6.1	2.0 ± 1.9	$2.1^{+3.5}_{-2.1}$
$e \rightsquigarrow \gamma$	21.5 ± 2.0	3.33 ± 0.62	3.75 ± 0.74	6.4 ± 1.1	5.7 ± 1.4	1.47 ± 0.25	1.24 ± 0.07
$VV\gamma$	44 ± 12	5.3 ± 1.6	5.8 ± 1.7	6.4 ± 1.8	5.7 ± 1.9	3.30 ± 0.97	27.3 ± 6.4
$t\bar{t}, t\bar{t}\gamma$, single t	42 ± 15	4.3 ± 1.5	3.4 ± 1.2	3.6 ± 1.2	2.13 ± 0.80	0.50 ± 0.18	0.63 ± 0.22
$W\gamma$	3.3 ± 1.5	0.39 ± 0.18	1.18 ± 0.55	–	0.04 ± 0.02	–	–
$t\bar{t}H, VH$	0.15 ± 0.02	0.03 ± 0.01	0.04 ± 0.01	0.06 ± 0.01	0.09 ± 0.03	0.02 ± 0.01	$0.17^{+0.18}_{-0.17}$
Pre-fit SM background	900 ± 120	90 ± 35	65 ± 27	53 ± 24	35 ± 22	7.8 ± 4.4	24 ± 4.7
Signal ($ZH \to \gamma\gamma_d$)	5.1 ± 1.3	1.98 ± 0.51	3.2 ± 1.0	5.5 ± 1.6	11.1 ± 3.1	14.9 ± 1.9	–

included as nuisance parameters, which are constrained by Gaussian distributions centered at zero with width equal to the corresponding uncertainty.

The dominant backgrounds, fake E_T^{miss} and electron faking photons are included in the fit taking the normalization from data-driven estimates described in Section 6. To model the BDT shape in the fit, simulated events are used for fake E_T^{miss}, while for the background with an electron faking a photon data from the probe-electron CR (e_p-CR) is considered after re-scaling each event by the appropriate fake rate $f_{e \rightsquigarrow \gamma}$.

The systematic uncertainties from data-driven methods are included in the fit as correlated among different BDT bins, as well as other experimental and theoretical systematic variations.

Two different fits are performed. The first corresponds to the background-only fit, in which the background predictions are determined in a fit to data assuming the presence of no signal. The second configuration instead allows for the presence of a specific signal and it is referred to as the model-dependent fit.

The results of the background-only fit are shown in Table 6, where observed and expected event yields are shown for all of the background processes considered in this analysis. The normalisation $k_{VV\gamma}$ factor is found to be 1.35 ± 0.38. The pre-fit and post-fit distributions of the BDT classifier response are shown in Figure 5. Post-fit uncertainties are reduced thanks to the constraints on nuisance parameters, in particular the ones related to the fake E_T^{miss}-induced background. Pre-fit distribution of m_T is also shown in Figure 6, being one of the most discriminant variables entering the BDT classifier.

The relative impact of each source of systematic uncertainty on the SM background estimates is summarised in Table 7. The purely statistical uncertainty of simulated samples is dominant, except in the last BDT bin, varying from about 3% to 16%. The largest systematic uncertainties in the last BDT bin are related to the shape of fake E_T^{miss} and to the jet energy scale and resolution corresponding respectively to 18% and 13%; uncertainty due to energy scale and resolution of electrons and photons corresponds to 5.6%, while the same uncertainty for muons corresponds to 4.1%. The other experimental and theoretical systematic uncertainties have a relative impact below about 3.5% in all BDT bins.
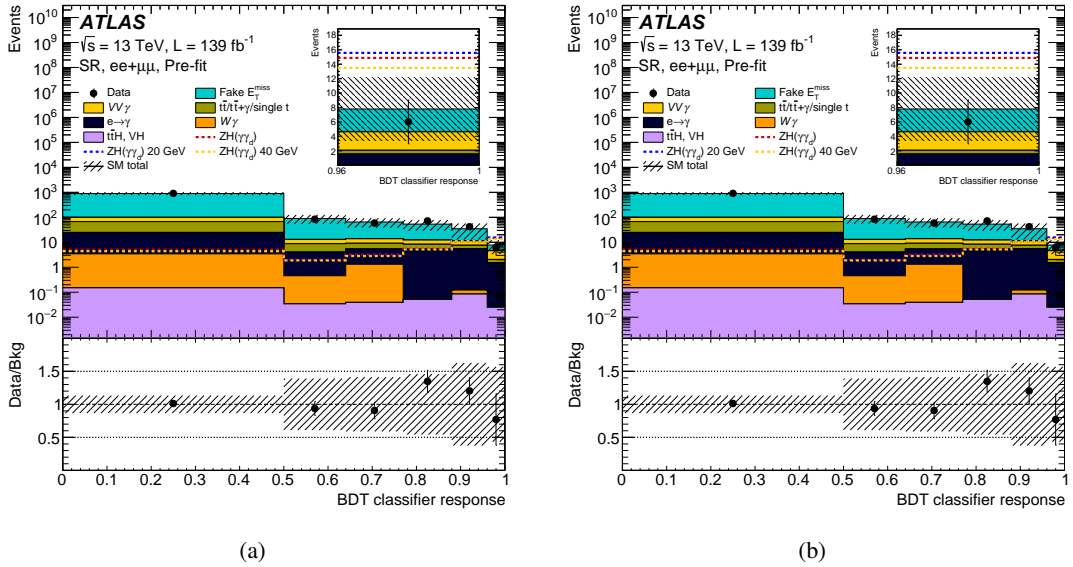
Figure 5: Distribution of the BDT classifier response in data and for the expected SM background before (a) and after (b) the background-only fit. The expectations for $ZH, H \to \gamma\gamma_d$ are also shown for the massless dark photon (red dashed line) and for dark photon mass values of 20 GeV (blue dashed line) and 40 GeV (yellow dashed line), assuming $\mathrm{BR}(H \to \gamma\gamma_d) = 5\%$. A zoomed view of the last BDT bin with linear y-axis scale is also shown. Uncertainties shown are statistical for data, while for backgrounds include statistical and systematic sources determined by the multiple-bin fit. The lower panel shows the ratio of data to expected background event yields.
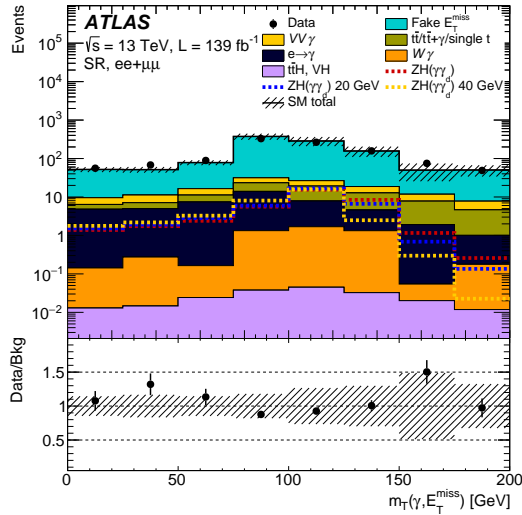

Figure 6: Distribution of m_T in data and for the expected SM background before the background-only fit. The expectations for $ZH, H \to \gamma\gamma_d$ are also shown for the massless dark photon (red dashed line) and for dark photon mass values of 20 GeV (blue dashed line) and 40 GeV (yellow dashed line), assuming $\mathrm{BR}(H \to \gamma\gamma_d) = 5\%$. Uncertainties shown are statistical for data, while for backgrounds include statistical and systematic sources determined by the multiple-bin fit. The lower panel shows the ratio of data to expected background event yields.

Table 7: Summary of the relative uncertainties in the background estimate for the BDT bins after the background-only fit. The individual uncertainties can be correlated and do not necessarily add in quadrature to equal the total background uncertainty.

BDT bin	0 - 0.50	0.50 - 0.64	0.64 - 0.77	0.77- 0.88	0.88 - 0.96	0.96 - 1
	[%]	[%]	[%]	[%]	[%]	[%]
Total (statistical+systematic) uncertainty	3.1	10	12	11	15	28
Statistical uncertainty	3.1	9.9	12	11	14	16
Fake $E_{\mathrm{T}}^{\mathrm{miss}}$ shape	0.17	0.97	0.40	0.55	2.8	18
Jet E scale and resolution	0.02	3.3	2.1	0.47	2.1	13
Electron, photon E scale and resolution	0.04	0.45	0.75	0.46	1.7	5.6
Muon E scale and resolution	0.08	0.17	0.15	0.91	1.2	4.1
Fake $E_{\mathrm{T}}^{\mathrm{miss}}$ data-driven	0.50	0.28	0.18	0.04	0.40	3.5
$E_{\mathrm{T}}^{\mathrm{miss}}$ soft term scale and resolution	0.26	0.16	0.59	0.49	0.20	2.8
Electron trigger/ID/iso/reco eff.	0.01	0.10	0.10	0.01	0.17	1.0
Muon trigger/ID/iso/reco eff.	0.01	0.07	0.08	0.06	0.03	0.84
Flavour tagging eff.	< 0.01	0.08	0.10	0.04	0.02	0.82
Electrons faking photons data-driven	0.02	0.08	0.06	0.06	0.07	0.73
Photon ID/iso/reco eff.	0.01	0.07	0.08	0.04	0.09	0.61
Reweighting of $\langle\mu\rangle$ in MC simulation	0.08	0.10	0.32	0.46	0.09	0.48
Top normalization	0.08	0.06	0.06	0.02	0.09	0.13
Theoretical $VV\gamma$	0.04	0.02	0.16	0.04	0.13	0.49
Theoretical fake $E_{\mathrm{T}}^{\mathrm{miss}}$	0.05	0.11	0.12	0.22	0.29	0.45
Theoretical top	0.09	0.05	0.17	0.10	0.04	0.28
Theoretical $W\gamma$	0.04	0.10	0.18	0.05	0.13	0.24
Theoretical Higgs	0.01	0.05	0.04	0.02	0.08	0.05

The event yields in data are consistent with the predicted SM background event yields, as shown in Table 6. The model-dependent fit is therefore performed in order to extract upper limits at 95% CL on the branching ratio of the sought decay mode of the Higgs boson. These limits are based on the profile-likelihood-ratio test statistic [80] and CL$_{\mathrm{s}}$ prescriptions [81], evaluated using the asymptotic approximation [82]. The fit is performed including the signal component of the Higgs boson production in ZH with subsequent Higgs boson decays into γ and γ_d. The results are provided for the massless dark photon, as well as for low dark photon mass values up to 40 GeV, as shown in Figure 7. The corresponding values are also reported in Table 8. The observed (expected) upper limits on BR(H$\to \gamma\gamma_d$) is at the level of 2.3% (2.8%), for massless γ_d and varies slightly until mass values of 20 GeV. The mass dependence of the limits become stronger beyond that value and the observed (expected) upper limit increases to about 2.5% (3.1%) at 40 GeV.

9 Conclusion

A search for dark photon candidates arising from semi-visible Standard Model Higgs boson decay $H \to \gamma\gamma_d$ is performed. The Higgs boson production in association with a $Z(\to \ell^+\ell^-)$ boson is exploited, which benefits from a relatively clean signal and high-efficiency lepton triggers. The search uses pp collision data collected by the ATLAS experiment at a centre-of-mass energy of $\sqrt{s} = 13$ TeV between 2015 and 2018 and corresponding to an integrated luminosity of 139 fb^{-1}. Data-driven techniques are optimized to estimate the main backgrounds from processes characterized by fake $E_{\mathrm{T}}^{\mathrm{miss}}$ and electrons misidentified
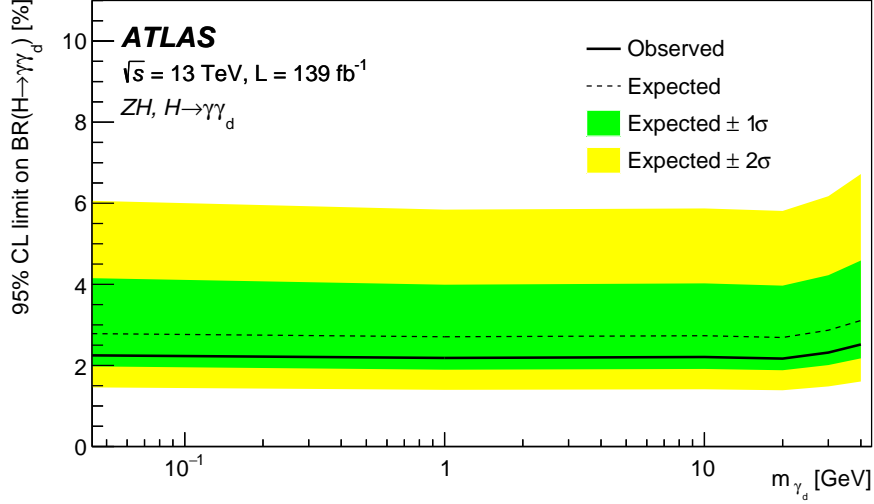
Figure 7: Observed and expected exclusion limits at 95% CL on BR($H \rightarrow \gamma\gamma_d$) as function of the γ_d mass. The green and yellow bands show respectively the $\pm 1\sigma$ and $\pm 2\sigma$ uncertainties.

Table 8: Observed and expected limits at 95% CL on BR($H \rightarrow \gamma\gamma_d$) for different values of the γ_d mass for the $ee + \mu\mu$ channel. The asymmetric error corresponds to the $\pm 1\sigma$

m_{γ_d}	BR($H \rightarrow \gamma\gamma_d$)$^{95\% \text{ CL}}_{\text{obs}}$	BR($H \rightarrow \gamma\gamma_d$)$^{95\% \text{ CL}}_{\text{exp}}$
[GeV]	[%]	[%]
0	2.28	$2.82^{+1.33}_{-0.84}$
1	2.19	$2.71^{+1.28}_{-0.81}$
10	2.21	$2.73^{+1.31}_{-0.82}$
20	2.17	$2.69^{+1.29}_{-0.81}$
30	2.32	$2.87^{+1.36}_{-0.86}$
40	2.52	$3.11^{+1.48}_{-0.93}$

as photons, while the normalization of the irreducible background is obtained using MC simulations constrained by data in a dedicated control region.

The sensitivity of the search is enhanced thanks to a Boosted Decision Tree algorithm that permits the construction of the discriminant kinematic observable. No excess of events above the SM expectation is found. Therefore, limits on the branching ratio of a SM Higgs boson decaying to a photon and a dark photon can be set. For massless γ_d, an observed (expected) upper limit on BR($H \rightarrow \gamma\gamma_d$) of 2.28% ($2.82^{+1.33}_{-0.84}$%) is set at 95% CL. For massive γ_d, the observed (expected) upper limits are found to be within the [2.19,2.52]% ([2.71,3.11]%) range for masses spanning from 1 GeV to 40 GeV.

References

[1] D. Clowe et al., *A direct empirical proof of the existence of dark matter*, The Astrophysical Journal **648** (2006) L109, arXiv: `astro-ph/0608407 [astro-ph]`.

[2] M. Fabbrichesi, E. Gabrielli and G. Lanfranchi, *The Physics of the Dark Photon*, 2021, arXiv: `2005.01515v3 [hep-ph]`.

[3] P. Fayet, *Extra U(1)'s and new forces*, Nucl. Phys. B **347** (1990) 743.

[4] H. Georgi, P. Ginsparg and S. L. Glashow, *Photon oscillations and cosmic background radiation*, Nature **306** (1983) 765.

[5] M. Raggi and V. Kozhuharov, *Results and perspectives in dark photon physics*, Riv. Nuovo Cim **38** (2015) 449.

[6] M. A. Deliyergiyev, *Recent Progress in Search for Dark Sector Signatures*, Open Phys. **14** (2015) 281, arXiv: `1510.06927 [hep-ph]`.

[7] P. Harris, P. Schuster and J. Zupan, *Snowmass White Paper: New flavors and rich structures in dark sectors*, (2022), arXiv: `2207.08990 [hep-ph]`.

[8] F. Curciarello, *Review on Dark Photon*, Eur. Phys. J. Conf. **118** (2016) 01008.

[9] J. Beacham et al., *Physics beyond colliders at CERN: beyond the Standard Model working group report*, J. Phys. G: Nucl. Part. Phys. **47** (2020) 010501, arXiv: `1901.09966 [hep-ex]`.

[10] J. Fan, A. Katz, L. Randall and M. Reece, *Dark-Disk Universe*, Phys. Rev. Lett. **110** (2013) 211302, arXiv: `1303.3271 [hep-ph]`.

[11] N. Arkani-Hamed, D. P. Finkbeiner, M. Recce and N. Weiner, *A theory of dark matter*, Phys. Rev. D **79** (2009) 015014, arXiv: `0810.0713 [hep-ph]`.

[12] E. Gabrielli, M. Heikinheimo, B. Mele and M. Raidal, *Dark photons and resonant monophoton signatures in Higgs boson decays at the LHC*, Phys. Rev. D **90** (2014) 055032, arXiv: `1405.5196 [hep-ph]`.

[13] S. Biswas, E. Gabrielli, M. Heikinheimo and B. Mele, *Dark-Photon searches via Higgs-boson production at the LHC*, Phys. Rev. D **93** (2016) 093011, arXiv: `1603.01377 [hep-ph]`.

[14] E. Gabrielli and M. Raidal, *Exponentially spread dynamical Yukawa couplings from non-perturbative chiral symmetry breaking in the dark sector*, Phys. Rev. D **89** (2014) 015008, arXiv: `1310.1090 [hep-ph]`.

[15] K. J. Kelly and Y.-D. Tsai, *Proton fixed-target scintillation experiment to search for millicharged dark matter*, Phys. Rev. D **100** (2019) 015043, arXiv: `1812.03998 [hep-ph]`.

[16] J. Jaeckel, M. Jankowiak and M. Spannowsky, *LHC probes the hidden sector*, 2013, arXiv: `1212.3620 [hep-ph]`.

[17] ATLAS Collaboration, *Search for dark matter in association with an energetic photon in pp collisions at $\sqrt{s} = 13$ TeV with the ATLAS detector*, JHEP **02** (2021) 226, arXiv: `2011.05259 [hep-ex]`.

[18] CMS Collaboration,
Search for new physics in the monophoton final state in proton–proton collisions at $\sqrt{s}$ = 13 TeV,
JHEP **10** (2017) 073, arXiv: 1706.03794 [hep-ex].

[19] ATLAS Collaboration, *Search for displaced photons produced in exotic decays of the Higgs boson using 13 TeV pp collisions with the ATLAS detector*, (2022), arXiv: 2209.01029 [hep-ex].

[20] CMS Collaboration, *Search for dark photons in decays of Higgs bosons produced in association with Z bosons in proton–proton collisions at $\sqrt{s}$ = 13 TeV*, JHEP **10** (2019) 139,
arXiv: 1908.02699 [hep-ex].

[21] CMS Collaboration, *Search for dark photons in Higgs boson production via vector boson fusion in proton–proton collisions at $\sqrt{s}$ = 13 TeV*, JHEP **03** (2021) 011, arXiv: 2009.14009 [hep-ex].

[22] ATLAS Collaboration, *Observation of electroweak production of two jets in association with an isolated photon and missing transverse momentum, and search for a Higgs boson decaying into invisible particles at 13 TeV with the ATLAS detector*, Eur. Phys. J. C **82** (2021) 105,
arXiv: 2109.00925 [hep-ex].

[23] ATLAS Collaboration, *The ATLAS Experiment at the CERN Large Hadron Collider*,
JINST **3** (2008) S08003.

[24] ATLAS Collaboration, *ATLAS Insertable B-Layer: Technical Design Report*,
ATLAS-TDR-19; CERN-LHCC-2010-013, 2010,
URL: https://cds.cern.ch/record/1291633, Addendum: ATLAS-TDR-19-ADD-1;
CERN-LHCC-2012-009, 2012, URL: https://cds.cern.ch/record/1451888.

[25] B. Abbott et al., *Production and integration of the ATLAS Insertable B-Layer*,
JINST **13** (2018) T05008, arXiv: 1803.00844 [physics.ins-det].

[26] ATLAS Collaboration, *Performance of the ATLAS trigger system in 2015*,
Eur. Phys. J. C **77** (2017) 317, arXiv: 1611.09661 [hep-ex].

[27] ATLAS Collaboration, *The ATLAS Collaboration Software and Firmware*,
ATL-SOFT-PUB-2021-001, 2021, URL: https://cds.cern.ch/record/2767187.

[28] ATLAS Collaboration, *ATLAS data quality operations and performance for 2015–2018 data-taking*,
JINST **15** (2020) P04003, arXiv: 1911.04632 [physics.ins-det].

[29] ATLAS Collaboration, *Performance of the ATLAS muon triggers in Run 2*,
JINST **15** (2020) P09015, arXiv: 2004.13447 [hep-ex].

[30] ATLAS Collaboration, *Performance of electron and photon triggers in ATLAS during LHC Run 2*,
Eur. Phys. J. C **80** (2020) 47, arXiv: 1909.00761 [hep-ex].

[31] ATLAS Collaboration, *Operation of the ATLAS trigger system in Run 2*, JINST **15** (2020) P10004,
arXiv: 2007.12539 [hep-ex].

[32] ATLAS Collaboration, *The ATLAS Simulation Infrastructure*, Eur. Phys. J. C **70** (2010) 823,
arXiv: 1005.4568 [physics.ins-det].

[33] S. Agostinelli et al., *GEANT4: A Simulation toolkit*, Nucl. Instrum. Meth. A **506** (2003) 250.

[34] T. Sjöstrand, S. Mrenna and P. Z. Skands, *A brief introduction to PYTHIA 8.1*,
Comput. Phys. Commun. **178** (2008) 852, arXiv: 0710.3820 [hep-ph].

[35] ATLAS Collaboration, *The Pythia 8 A3 tune description of ATLAS minimum bias and inelastic measurements incorporating the Donnachie–Landshoff diffractive model*,
ATL-PHYS-PUB-2016-017, 2016, URL: https://cds.cern.ch/record/2206965.

[36] ATLAS Collaboration, *AtlFast3: The Next Generation of Fast Simulation in ATLAS*,
Comput. Softw. Big Sci. **6** (2022), arXiv: 2109.02551 [hep-ex].

[37] T. Gleisberg et al., *Event generation with SHERPA 1.1*, JHEP **02** (2009) 007,
arXiv: 0811.4622 [hep-ph].

[38] D. J. Lange, *The EvtGen particle decay simulation package*,
Nucl. Instrum. Meth. A **462** (2001) 152.

[39] D. de Florian et al.,
Handbook of LHC Higgs Cross Sections: 4. Deciphering the Nature of the Higgs Sector, (2016),
arXiv: 1610.07922 [hep-ph].

[40] J. M. Campbell et al., *NLO Higgs boson production plus one and two jets using the POWHEG BOX,
MadGraph4 and MCFM*, JHEP **07** (2012) 092, arXiv: 1202.5475 [hep-ph].

[41] G. Luisoni, P. Nason, C. Oleari and F. Tramontano, *$HW^\pm/HZ + 0$ and 1 jet at NLO with the
POWHEG BOX interfaced to GoSam and their merging within MiNLO*, JHEP **10** (2013) 083,
arXiv: 1306.2542 [hep-ph].

[42] R. D. Ball et al., *Parton distributions for the LHC run II*, JHEP **04** (2015) 040,
arXiv: 1410.8849 [hep-ph].

[43] J. Pumplin et al.,
New Generation of Parton Distributions with Uncertainties from Global QCD Analysis,
JHEP **07** (2002) 012, arXiv: hep-ph/0201195.

[44] S. Goria, G. Passarino and D. Rosco, *The Higgs-boson lineshape*, Nucl. Phys. B **864** (2012) 530,
arXiv: 1112.5517 [hep-ph].

[45] L. Carloni and T. Sjöstrand, *Visible effects of invisible Hidden Valley radiation*,
Journal of High Energy Physics **2010** (2010), arXiv: 1006.2911 [hep-ph].

[46] K. Melnikov and F. Petriello,
Electroweak gauge boson production at hadron colliders through $O(\alpha_s^2)$,
Phys. Rev. D **74** (2006) 114017, arXiv: hep-ph/0609070.

[47] LHCTopWG, *NNLO+NNLL top-quark-pair cross sections*, 2015,
URL: https://twiki.cern.ch/twiki/bin/view/LHCPhysics/TtbarNNLO.

[48] LHCTopWG, *NLO single-top channel cross sections*, 2017,
URL: https://twiki.cern.ch/twiki/bin/view/LHCPhysics/SingleTopRefXsec.

[49] E. Bothmann et al., *Event generation with Sherpa 2.2*, SciPost Phys. **7** (2019) 034,
arXiv: 1905.09127 [hep-ph].

[50] T. Gleisberg and S. Höche, *Comix, a new matrix element generator*, JHEP **12** (2008) 039,
arXiv: 0808.3674 [hep-ph].

[51] F. Cascioli, P. Maierhöfer and S. Pozzorini, *Scattering Amplitudes with Open Loops*,
Phys. Rev. Lett. **108** (2012) 111601, arXiv: 1111.5206 [hep-ph].

[52] S. Schumann and F. Krauss,
A parton shower algorithm based on Catani–Seymour dipole factorisation, JHEP **03** (2008) 038,
arXiv: 0709.1027 [hep-ph].

[53] S. Höche, F. Krauss, M. Schönherr and F. Siegert,
QCD matrix elements + parton showers. The NLO case, JHEP **04** (2013) 027,
arXiv: 1207.5030 [hep-ph].

[54] T. Sjöstrand et al., *An introduction to PYTHIA 8.2*, Comput. Phys. Commun. **191** (2015) 159, arXiv: 1410.3012 [hep-ph].

[55] L. Lönnblad and S. Prestel, *Matching tree-level matrix elements with interleaved showers*, JHEP **2012** (2012), ISSN: 1029-8479, arXiv: 1109.4829v3 [hep-ex].

[56] S. Frixione, *Isolated photons in perturbative QCD*, Phys. Lett. B **429** (1998) 369, arXiv: hep-ph/9801442.

[57] S. Frixione, E. Laenen, P. Motylinski, C. White and B. R. Webber, *Single-top hadroproduction in association with a W boson*, JHEP **07** (2008) 029, arXiv: 0805.3067 [hep-ph].

[58] J. Alwall et al., *The automated computation of tree-level and next-to-leading order differential cross sections, and their matching to parton shower simulations*, JHEP **07** (2014) 079, arXiv: 1405.0301 [hep-ph].

[59] ATLAS Collaboration, *Vertex Reconstruction Performance of the ATLAS Detector at $\sqrt{s} = 13$ TeV*, ATL-PHYS-PUB-2015-026, 2015, URL: https://cds.cern.ch/record/2037717.

[60] ATLAS Collaboration, *Electron and photon performance measurements with the ATLAS detector using the 2015–2017 LHC proton–proton collision data*, JINST **14** (2019) P12006, arXiv: 1908.00005 [hep-ex].

[61] ATLAS Collaboration, *Muon reconstruction and identification efficiency in ATLAS using the full Run 2 pp collision data set at $\sqrt{s} = 13$ TeV*, Eur. Phys. J. C **81** (2021) 578, arXiv: 2012.00578 [hep-ex].

[62] M. Cacciari, G. P. Salam and G. Soyez, *The anti-k_t jet clustering algorithm*, JHEP **04** (2008) 063, arXiv: 0802.1189 [hep-ph].

[63] M. Cacciari, G. P. Salam and G. Soyez, *FastJet user manual*, Eur. Phys. J. C **72** (2012) 1896, arXiv: 1111.6097 [hep-ph].

[64] ATLAS Collaboration, *Jet reconstruction and performance using particle flow with the ATLAS Detector*, Eur. Phys. J. C **77** (2017) 466, arXiv: 1703.10485 [hep-ex].

[65] ATLAS Collaboration, *Jet energy scale and resolution measured in proton–proton collisions at $\sqrt{s} = 13$ TeV with the ATLAS detector*, Eur. Phys. J. C **81** (2020) 689, arXiv: 2007.02645 [hep-ex].

[66] ATLAS Collaboration, *Tagging and suppression of pileup jets with the ATLAS detector*, ATLAS-CONF-2014-018, 2014, URL: https://cds.cern.ch/record/1700870.

[67] ATLAS Collaboration, *Forward Jet Vertex Tagging: A new technique for the identification and rejection of forward pileup jets*, ATL-PHYS-PUB-2015-034, 2015, URL: https://cds.cern.ch/record/2042098.

[68] ATLAS Collaboration, *Forward jet vertex tagging using the particle flow algorithm*, ATL-PHYS-PUB-2019-026, 2019, URL: https://cds.cern.ch/record/2683100.

[69] ATLAS Collaboration, *Measurements of b-jet tagging efficiency with the ATLAS detector using $t\bar{t}$ events at $\sqrt{s} = 13$ TeV*, JHEP **08** (2018) 089, arXiv: 1805.01845 [hep-ex].

[70] ATLAS Collaboration, *Performance of missing transverse momentum reconstruction with the ATLAS detector using proton–proton collisions at $\sqrt{s}$ = 13 TeV*, Eur. Phys. J. C **78** (2018) 903, arXiv: 1802.08168 [hep-ex].

[71] ATLAS Collaboration, *Object-based missing transverse momentum significance in the ATLAS Detector*, ATLAS-CONF-2018-038, 2018, URL: https://cds.cern.ch/record/2630948.

[72] ATLAS Collaboration, *Selection of jets produced in 13 TeV proton–proton collisions with the ATLAS detector*, ATLAS-CONF-2015-029, 2015, URL: https://cds.cern.ch/record/2037702.

[73] T. Chen and C. Guestrin, *XGBoost: A Scalable Tree Boosting System*, CoRR (2016), arXiv: 1603.02754 [cs.LG].

[74] ATLAS Collaboration, *Luminosity determination in pp collisions at $\sqrt{s}$ = 13 TeV using the ATLAS detector at the LHC*, ATLAS-CONF-2019-021, 2019, URL: https://cds.cern.ch/record/2677054.

[75] G. Avoni et al., *The new LUCID-2 detector for luminosity measurement and monitoring in ATLAS*, JINST **13** (2018) P07017.

[76] ATLAS Collaboration, *Measurement of the photon identification efficiencies with the ATLAS detector using LHC Run 2 data collected in 2015 and 2016*, Eur. Phys. J. C **79** (2019) 205, arXiv: 1810.05087 [hep-ex].

[77] ATLAS Collaboration, *Tagging and suppression of pileup jets*, ATL-PHYS-PUB-2014-001, 2014, URL: https://cds.cern.ch/record/1643929.

[78] ATLAS Collaboration, *Optimisation and performance studies of the ATLAS b-tagging algorithms for the 2017-18 LHC run*, ATL-PHYS-PUB-2017-013, 2017, URL: https://cds.cern.ch/record/2273281.

[79] ATLAS Collaboration, *Deep Sets based Neural Networks for Impact Parameter Flavour Tagging in ATLAS*, ATL-PHYS-PUB-2020-014, 2020, URL: https://cds.cern.ch/record/2718948.

[80] M. Baak et al., *HistFitter software framework for statistical data analysis*, Eur. Phys. J. C**75** (2015) 153, arXiv: 1410.1280 [hep-ex].

[81] A. L. Read, *Presentation of search results: the CL_s technique*, J. Phys. G **28** (2002) 2693.

[82] G. Cowan, K. Cranmer, E. Gross and O. Vitells, *Asymptotic formulae for likelihood-based tests of new physics*, Eur. Phys. J. C **71** (2011) 1554, arXiv: 1007.1727 [physics.data-an], Erratum: Eur. Phys. J. C **73** (2013) 2501.